Analysis and Compensation for Systematical Errors in Airborne Microwave Photonic SAR Imaging by 2-D Autofocus

Min Chen, Xiaolan Qiu, *Senior Member, IEEE*, Ruoming Li, *Senior Member, IEEE*, Wangzhe Li, *Member, IEEE*, and Kun Fu, *Senior Member, IEEE*

***Abstract*—In the area of synthetic aperture radar (SAR), the ultrahigh resolution is always a continuous pursuit for researchers. To realize ultrahigh resolution, microwave photonics technology is an excellent solution since it has advantages of low transmission loss, ultrawide bandwidth (UWB), etc. However, with the improvement of resolution, new problems arise as the impact of more systematical errors becomes non-negligible, for example, the synchronization error between the transmit channel and the mixing channel, unknown system delay during signal reception, and the fluctuation of frequency for UWB signals. These factors will bring the degradation of the focusing quality of SAR images together with the motion errors and the trajectory measurement errors, causing not only residual range cell migration and azimuth phase error, but also higher order phase error along the range frequency dimension. In this article, we discuss the adverse influence of the above factors and give a detailed analysis of the 2-D phase error of the coarse focused image processed by range migration algorithm. Then, to compensate for the above unknown systematical errors, a 2-D autofocus method is proposed, and the effectiveness is validated by experiments on both simulated and real data.**

***Index Terms*—2-D autofocus, microwave photonic (MWP) synthetic aperture radar (SAR), range migration algorithm (RMA), systematical errors, ultrawide bandwidth (UWB).**

I. Introduction

SYNTHETIC aperture radar (SAR) is an active means of aerospace remote sensing, which can operate day and night and is rarely limited by the weather. It can achieve high resolution in both azimuth and range dimensions simultaneously [1]. On the one hand, it realizes high azimuth resolution by coherently processing the signal sequence within the length of a synthetic aperture. On the other hand, it obtains high range resolution relying on the large bandwidth of the transmitted signal. Therefore, with the increasing demand for resolution, the requirement for large-bandwidth signals is inevitable, which brings challenges to both hardware and algorithms. Owing to the electronic bottleneck, it is difficult for traditional electronic methods to generate ultrawide-bandwidth (UWB) signals that meet the requirements of high resolution. While microwave photonics (MWP) technology is an excellent alternative method that can generate and process large-bandwidth signals [2], [3], [4]. Besides, compared to conventional electronics technology, MWP technology has the advantages of low transmission loss, light weight, small size, and so on [2], [5], [6].

The significant increase in the resolution of MWP SAR determines that it is more sensitive to various errors. First, for airborne MWP SAR, the compensation for motion errors caused by the circumstance, such as atmospheric turbulence and platform vibration, is critical to final image quality. For a system with a bandwidth of 5.72 GHz, a trajectory deviation of only 10 cm along the slant range will cause migration of almost four range cells in the raw data. Second, for the MWP SAR system, the frequency-modulated continuous-wave (FMCW) and dechirp-on-receive technologies are commonly adopted [7]. And we generally assume that for such a system, the transmit channel, the mixing channel, and the receive channel are synchronized. However, in the actual situation, there is an inevitable difference between these channels. For example, a synchronous error of 0.067 μs corresponds to a slant range error of about 10 m, which can cause severe defocusing. Third, owing to the sensitivity of optical devices [8], which are widely used in the MWP SAR system, the unknown system delay may also be induced during signal reception. Besides, compared to conventional SAR systems, the bandwidth of MWP SAR is ultrawide, so the fluctuation of frequency for UWB signals is an important factor that may cause the degradation of imaging quality and must be taken into account. The latter three types of errors are all caused by the SAR system itself, so we refer to them as systematical errors. So far, most of the existing autofocus methods focused on the influence of motion errors, but only a few

Manuscript received 21 November 2022; revised 31 December 2022 and 3 February 2023; accepted 13 February 2023. Date of publication 16 February 2023; date of current version 2 March 2023. This work was supported by the National Key R&D Program of China under Grant 2018YFA0701903. *(Corresponding author: Xiaolan Qiu.)*

Min Chen is with the Key Laboratory of Technology in Geo-Spatial Information Processing and Application Systems, Chinese Academy of Sciences, Beijing 100190, China, also with the Aerospace Information Research Institute, Chinese Academy of Sciences, Beijing 100094, China, and also with the School of Electronic, Electrical and Communication Engineering, University of Chinese Academy of Sciences, Beijing 100049, China (e-mail: chenmin20@mails.ucas.ac.cn).

Xiaolan Qiu and Kun Fu are with the Suzhou Aerospace Information Research Institute, Suzhou 215124, China, and also with the Aerospace Information Research Institute, Chinese Academy of Sciences, Beijing 100094, China (e-mail: xlqiu@mail.ie.ac.cn; fukun@mail.ie.ac.cn).

Ruoming Li and Wangzhe Li are with the National Key Laboratory of Microwave Imaging Technology, Aerospace Information Research Institute, Chinese Academy of Sciences, Beijing 100190, China (e-mail: rmli@mail.ie.ac.cn; wzli@mail.ie.ac.cn).

Digital Object Identifier 10.1109/JSTARS.2023.3245827

concerned the systematical errors [9]. Therefore, for MWP SAR, it is demanding to develop an imaging method that takes the unknown systematical errors into consideration and is capable of compensating for them.

For SAR imaging, which is essentially a 2-D focusing process, lots of mature algorithms already exist. In particular, for airborne SAR with ultrahigh resolution, since there are trajectory deviations, the selection of proper imaging algorithms is of great importance. The backprojection algorithm (BPA) [10] is the most accurate algorithm since it does not involve any assumption or approximation. However, it is a point-by-point processing method that results in a large computational complexity and low efficiency. The chirp scaling algorithm (CSA) [11] is an efficient frequency-domain imaging algorithm, but due to the approximations taken during processing, its ability to deal with ultrahigh-resolution situations is limited. Although there are some modified versions of CSA, such as nonlinear chirp scaling [12], [13], extended nonlinear chirp scaling [14], [15], [16], etc., approximations still exist in these algorithms. The range migration algorithm (RMA) [17], [18], also called Omega-K algorithm, is another frequency-domain imaging algorithm; compared to the CSA, it is much more accurate and can be used for highly squinted situations since it does not adopt any approximation during the theoretical derivation. Besides, it is also more efficient compared to the BPA. Therefore, in this article, we choose RMA as the imaging algorithm.

For SAR autofocus, lots of autofocus methods have been developed. Generally, the negative effects induced by motion errors are mainly reflected in two aspects: residual range cell migration (RCM) and azimuth phase error (APE). For the estimation of residual RCM that corresponds to the first-order phase error in the range dimension, a common practice is to use the range alignment methods in inverse SAR for reference, which include methods based on cross correlation [19], [20] and methods based on image evaluation functions, such as the maximum contrast method and the minimum entropy method [21], [22]. As for the existing APE estimation methods, they can be classified into two categories: parametric and nonparametric [23]. The parametric methods mainly include mapdrift algorithm (MDA) and its modified versions [24], [25], [26], [27]. And the nonparametric ones are represented by the phase gradient algorithm (PGA) [28] and modifications based on it [29], [30], [31], [32]. However, in these conventional autofocus methods, only the range envelope error is concerned; in other words, the second-order and higher order phase errors in the range dimension are completely ignored. While for MWP SAR, the signal bandwidth is ultrawide, these high-order phase errors may lead to obvious defocus along the range dimension, which must be taken into account. In recent years, some novel 2-D autofocus methods have also been proposed. In [33] and [34], the analytical structure of the phase error is explored, and a semiblind method for 2-D phase error estimation and compensation is proposed, but they are based on the models considering only the motion errors. In [9], a 2-D autofocus strategy accounting for systematical errors in MWP SAR systems is developed. However, it just compensates for the range envelope error, i.e., first-order phase error in the range dimension, which is powerless to range defocus related to second-order and even higher order phase errors in the range dimension. Therefore, it is urgent to find a new autofocus method to improve the focusing quality of MWP SAR data considering all the factors mentioned above.

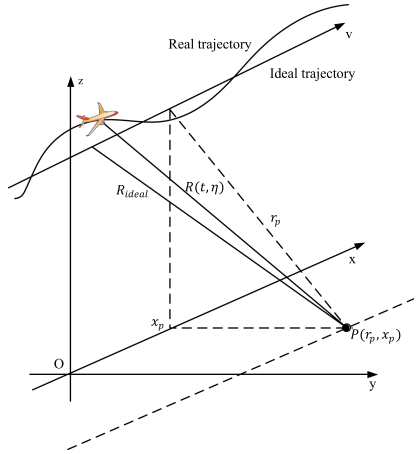

Fig. 1. Raw data acquisition geometry.

The main contributions of this article are as follows:

1) We set up the signal model considering the unknown systematical errors in addition to the inevitable motion errors for airborne MWP SAR imaging and conduct a detailed analysis of the influence of those unknown systematical errors, including synchronization error during signal mixing, unknown system delay, and the fluctuation of signal frequency.
2) Based on the theoretical analysis, we propose a 2-D autofocus method to compensate for these systematical errors by exploiting the structural property of the 2-D phase error motivated by the knowledge-aided 2-D autofocus method proposed in [33] and [34]. The experiments on both simulated and real data validate the superior performance of the proposed method.

The rest of this article is organized as follows. In Section II, the signal model is established considering the three kinds of systematical errors mentioned earlier. Then, the 2-D phase error of the coarse focused image processed by the RMA is obtained. In Section III, the structural property and the space-variant property of the phase error are discussed. The new 2-D autofocus method is described in Section IV. In Section V, results of simulated and real data are presented to validate the effectiveness of the proposed method. Finally, Section VI concludes this article.

II. 2-D Phase Error Model for the RMA

A. Ideal FMCW Signal Model

Fig. 1 shows the raw data acquisition geometry, where the straight line parallel to x is the ideal trajectory of the SAR platform, and the curve represents the actual trajectory during data acquisition. For an arbitrary target P within the scene, let r_p represent the minimum slant range between the antenna phase center (APC) and P, and x_p be the azimuth position of P. Then, the instantaneous slant range between APC and P can

be described as

$$R(t,\eta)=\sqrt{r_p^2+(v\eta+vt-x_p)^2}+\Delta R(t,\eta) \quad (1)$$

where η is the slow time, t is the fast time, v is the mean velocity of the radar platform along the x-direction, the first term on the right-hand side of the equation is the ideal instantaneous slant range, that is R_{ideal} in Fig. 1, and $\Delta R(t,\eta)$ represents the range error resulted from trajectory deviation. Different from the conventional pulse SAR system, the FMCW SAR system transmits electromagnetic signals continuously, so the stop-and-go assumption does not hold anymore, which means that the motion within the sweep, i.e., the vt term, must be taken into consideration.

With (1), the received signal can be written as

$$s_r(t,\eta)=\exp\left\{-j\left[2\pi f_0(t-t_p)+\pi k_r(t-t_p)^2\right]\right\} \quad (2)$$

where f_0 and k_r are the carrier frequency and frequency-modulated (FM) rate of the transmitted signal, respectively. t_p is often called round-trip time, and it can be expressed as

$$t_p=\frac{2R(\eta,t)}{c} \quad (3)$$

where c is the speed of light. In (2), we ignore the amplitude factors related to the antenna pattern, the transmitted signal envelope, and so on.

For the FMCW system, the dechirp-on-receive technology is generally adopted in order to reduce the sampling requirements [7]. The dechirp process is developed by mixing the received signal in (2) with a reference signal and, then, feeding the output of the mixer into a low-pass filter. If we take the conjugate of the transmitted signal as the reference signal, that is

$$s_{\text{ref}}(t,\eta)=\exp\left\{j\left(2\pi f_0 t+\pi k_r t^2\right)\right\} \quad (4)$$

then the intermediate frequency signal can be written as

$$s_{\text{IF}}(t,\eta)=\exp\left\{j\left[2\pi(f_0+k_r t)t_p-\pi k_r t_p^2\right]\right\}. \quad (5)$$

The last exponential term is an undesirable term called residual video phase (RVP). It can be easily removed by range Fourier transformation (FT), phase multiplication, and range inverse FT [35]. After removing the RVP term, the signal is given by

$$s_{\text{IF}}(t,\eta)=\exp\left\{j2\pi(f_0+k_r t)t_p\right\} \quad (6)$$

where $f_0+k_r t$ is the range frequency.

B. Systematical Errors for MWP SAR

In the presence of systematical errors, which are caused by the three sources mentioned earlier, the signal model has to make some modifications. Fig. 2 shows the simplified signal flow diagram, where $s(t)$ and $s(t-t_p)$ represent the transmitted and received signals, respectively. $t=0$ is the time to start recording the signals. δt_1 and δt_2 are the synchronization errors of the transmit channel and the mixing channel, respectively. δt_3 is the unknown system delay error that occurs during signal reception. The lower part of Fig. 2 shows the time line of each signal. In the rest of this section, we first discuss the three types of errors separately and then consider the case where the three kinds of errors all exist.

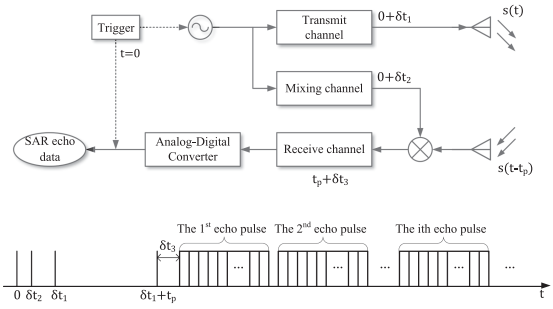

Fig. 2. Simplified signal flow diagram of the MWP SAR system.

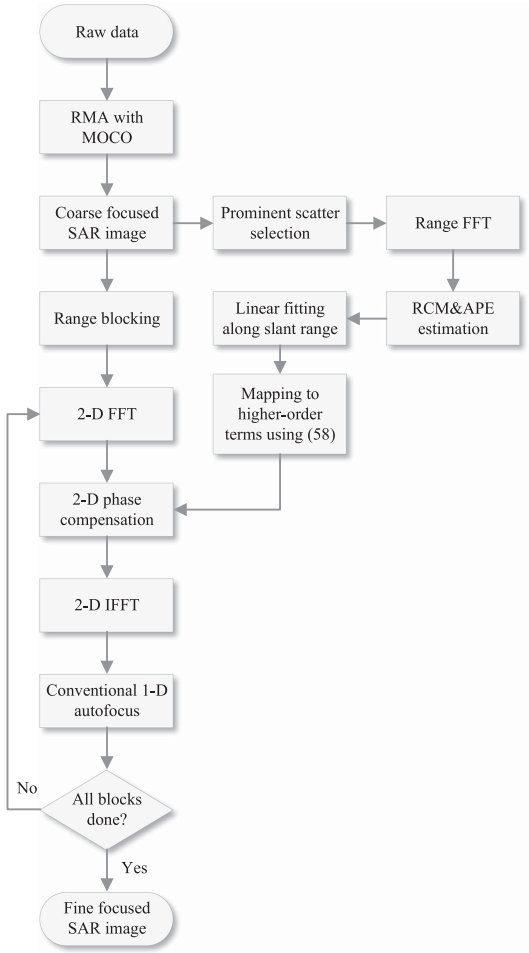

Fig. 3. Flowchart of the proposed 2-D autofocus method.

1) Synchronization Error During Signal Mixing: In the ideal signal model, we have made an implicit assumption that the transmit channel, the receive channel, and the mixing channel are synchronized. However, in most cases, the real system cannot meet this requirement. Suppose that the receive channel has an additional delay of δt_1, while the mixing channel has a different delay of δt_2. Then, with the synchronization errors δt_1 and δt_2, the phases of signals (2)–(6) turn into the following expressions.

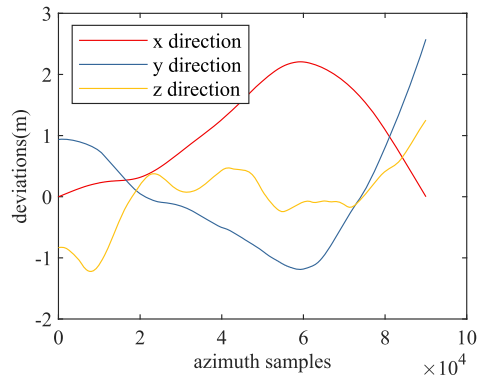

Fig. 4. Trajectory deviation of radar platform.

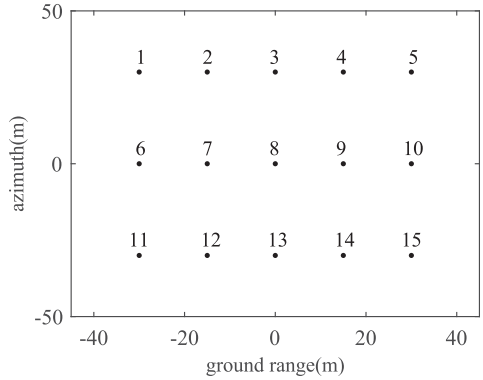

Fig. 5. Simulated scenario.

The phase of the received signal is

$$\varphi_r(t,\eta) = -2\pi f_0\left(t-\delta t_1-t_p\right)-\pi k_r\left(t-\delta t_1-t_p\right)^2. \quad (7)$$

The phase of the reference signal is

$$\varphi_{\text{ref}}\left(t,\eta\right) = 2\pi f_0\left(t-\delta t_2\right)+\pi k_r\left(t-\delta t_2\right)^2. \quad (8)$$

Ignoring the constant terms, the phase of the signal after mixing and low-pass filtering can be expressed as

$$\varphi_{\text{IF}}\left(t,\eta\right) = 2\pi\left(f_0+k_r\left(t-\delta t_1\right)\right)t_p-\pi k_r t_p^2 + 2\pi k_r(\delta t_1-\delta t_2)t. \quad (9)$$

The additional linear term of fast time t caused by the synchronization errors δt_1 and δt_2, i.e., the last term of (9), will affect the removal of RVP. That is to say, we cannot just simply remove the squared term, i.e., $\pi k_r t_p^2$, while leaving other terms unchanged. Taking the linear term into consideration and ignoring the unnecessary constant terms, the signal phase after removing RVP is given by

$$\varphi_{\text{IF}}\left(t,\eta\right) = 2\pi\left(f_0+k_r\left(t-\delta t_2\right)\right)t_p+2\pi k_r(\delta t_1-\delta t_2)t. \quad (10)$$

From the above equation, it can be seen that due to the delay δt_2, the range frequency changes from $f_0+k_r t$ into $f_0+k_r(t-\delta t_2)$, which is equivalent to a variation of the carrier frequency. Besides, δt_1 and δt_2 also induce an additional linear term of fast time t, which will affect the range positions of targets.

2) Unknown System Delay: The unknown system delay refers to the additional propagation delay in the receive channel, which is generally a constant value that corresponds to a propagation distance at a meter level. Suppose that the unknown system delay is δt_3 and consider the impact of δt_3 alone. By simply replacing t_p in (5) with $t_p+\delta t_3$, we can obtain the new expression of the phase of the signal after mixing and low-pass filtering, that is

$$\varphi_{\text{IF}}\left(t,\eta\right) = 2\pi\left(f_0+k_r t\right)\left(t_p+\delta t_3\right)-\pi k_r(t_p+\delta t_3)^2. \quad (11)$$

Then, the signal phase after removing RVP is given by

$$\varphi_{\text{IF}}\left(\eta,t\right) = 2\pi\left(f_0+k_r t\right)\left(t_p+\delta t_3\right). \quad (12)$$

It can be seen that the presence of the unknown system delay δt_3 also introduces an additional linear term of fast time t.

3) Inaccurate FM Rate: The FM rate of the transmitted signal is an important parameter for the imaging process. If it is not accurately known, defocus and geometric distortion will be anticipated in the final image [36]. Assume that the difference between the real FM rate and the given value is δk_r, which means

$$k_{\text{real}} = k_r+\delta k \quad (13)$$

where k_{real} is the real FM rate of the transmitted signal, k_r is the inaccurate value provided by the radar supplier, and δk_r is the FM rate error.

Considering the impact of FM rate error δk_r alone, the phase of the signal after mixing and low-pass filtering can be obtained by replacing k_r in (5) with $k_r+\delta k_r$, that is

$$\varphi_{\text{IF}}\left(t,\eta\right) = 2\pi\left(f_0+\left(k_r+\delta k\right)t\right)t_p-\pi\left(k_r+\delta k\right)t_p^2. \quad (14)$$

The additional linear term of fast time t induced by δk_r will also affect the removal of RVP and need to be taken into consideration. After removing RVP, the signal phase becomes

$$\varphi_{\text{IF}}\left(t,\eta\right) = 2\pi\left(f_0+\left(k_r+\delta k\right)t\right)t_p+\pi\left(\delta k+\frac{\delta k^2}{k}\right)t_p^2. \quad (15)$$

The last term is the residual RVP error caused by δk_r. Since its value is small, we will ignore this term in the following discussion. Then, the signal phase can be expressed as

$$\varphi_{\text{IF}}\left(t,\eta\right) = 2\pi\left(f_0+\left(k_r+\delta k\right)t\right)t_p. \quad (16)$$

Different from the synchronization error described earlier, which can be equivalent to an offset of carrier frequency, δk_r introduces a range frequency shift that is linear to the fast time t, which can be regarded as an offset of range baseband frequency.

4) Considering the Three Errors Above Simultaneously: Although the three types of errors discussed earlier are caused by different factors, their impact can be uniformly summarized as an offset of range frequency, both center frequency and baseband frequency, and an additional linear term of t. Therefore, it is straightforward to combine the three cases together. That is to say, consider the case where the synchronization errors δt_1 and δt_2, the unknown system delay δt_3, and the FM error δk all exist.

Under this condition, ignoring the insignificant constant terms, the phase of the signal after mixing and low-pass filtering

turns into

$$\begin{aligned}\varphi_{\mathrm{IF}}(t,\eta) = {} & 2\pi\left(f_0+(k_r+\delta k)\left(t-\delta t_1-\delta t_3\right)\right)t_p \\ & +2\pi\left(k_r+\delta k\right)\left(\delta t_1-\delta t_2+\delta t_3\right)t \\ & -\pi\left(k_r+\delta k\right)t_p^2. \end{aligned} \tag{17}$$

After applying the RVP removal process, the phase of the output signal is given by

$$\begin{aligned}\varphi_{\mathrm{IF}}(t,\eta) = {} & 2\pi\Bigg\{f_0+(k_r+\delta k)\cdot\Bigg[t-\Delta t-\delta t_2 \\ & +\left(1+\frac{\delta k}{k_r}\right)\Delta t\Bigg]\Bigg\}t_p+2\pi\left(k_r+\delta k\right)\Delta t\cdot t \end{aligned} \tag{18}$$

with $\Delta t=\delta t_1-\delta t_2+\delta t_3$. Note that, again, we ignore the nonessential constant terms. Besides, the residual RVP error, as described in (15), is also ignored.

Let $\tilde{f}_0$ be the real carrier frequency, which can be written as

$$\begin{aligned}\tilde{f}_0 &= f_0-\left(k_r+\delta k\right)\left[\Delta t+\delta t_2-\left(1+\frac{\delta k}{k_r}\right)\Delta t\right] \\ &= f_0-\Delta f_0 \end{aligned} \tag{19}$$

where

$$\Delta f_0=\left(k_r+\delta k\right)\left[\Delta t+\delta t_2-\left(1+\frac{\delta k}{k_r}\right)\Delta t\right] \tag{20}$$

represents the carrier frequency shift caused by errors, and f_0 is the ideal carrier frequency.

Let $\tilde{f}_\tau$ be the real range baseband frequency

$$\tilde{f}_\tau=\left(k_r+\delta k\right)t=\left(1+\frac{\delta k}{k_r}\right)f_\tau \tag{21}$$

where f_τ is the ideal range baseband frequency.

With (19) and (21), the signal phase in (18) can be simplified as

$$\tilde{\varphi}_{\mathrm{IF}}(\tilde{f}_\tau,\eta)=2\pi\left(\tilde{f}_0+\tilde{f}_\tau\right)t_p-2\pi\tilde{f}_\tau\Delta t \tag{22}$$

and then the signal before imaging can be expressed as

$$\tilde{s}_{\mathrm{IF}}(\tilde{f}_\tau,\eta)=\exp\left\{j2\pi\left[\left(\tilde{f}_0+\tilde{f}_\tau\right)t_p-\tilde{f}_\tau\Delta t\right]\right\}. \tag{23}$$

C. Range Migration Algorithm Analysis

In this part, we will deduce the change of signal phases during RMA, in detail. Assume that the trajectory is ideal, i.e., $\Delta R(t,\eta)=0$. For the more general case where the unknown trajectory error exists, we will discuss later.

1) Azimuth FT: For the FMCW SAR system that adopts the dechirp-on-receive technology, we can obtain the signal in the 2-D spatial frequency domain directly by performing azimuth FT operation on the signal after the removal of RVP, that is

$$\begin{aligned}S\left(\tilde{f}_\tau,f_a\right) &= \int\tilde{s}_{\mathrm{IF}}\cdot\exp\left\{-j2\pi f_a\eta\right\}d\eta \\ &= \int\exp\left\{j2\pi\left[\left(\tilde{f}_0+\tilde{f}_\tau\right)t_p-\tilde{f}_\tau\Delta t-f_a\eta\right]\right\}d\eta. \end{aligned} \tag{24}$$

Note that t_p is the round-trip time as shown in (3), which is dependent on both the fast time t and the slow time η.

In order to obtain the analytical expression of the integration in (24), we can resort to the principle of stationary phase (POSP) [1]. The first step of the POSP is to calculate the value of stationary phase (SP) point, which can be realized by making the first-order derivative of the integrated phase to the slow time equal to zero, that is

$$\frac{d}{d\eta}\left\{2\pi\left[\left(\tilde{f}_0+\tilde{f}_\tau\right)t_p-\tilde{f}_\tau\Delta t-f_a\eta\right]\right\}=0. \tag{25}$$

With (3) and (25), we can get the SP point as follows:

$$\eta^*=\frac{x_p}{v}+\frac{r_p\cdot f_a\cdot c}{2v^2\sqrt{\left(\tilde{f}_0+\tilde{f}_\tau\right)^2-\left(\frac{cf_a}{2v}\right)^2}}-t \tag{26}$$

where the last term $-t$ is due to the motion within the sweep, which can be compensated easily by phase multiplication. The instantaneous range distance at the moment of SP point can be written as

$$R\left(\eta^*,\tau\right)=\frac{r_p}{\sqrt{1-\left(\frac{cf_a}{2v\left(\tilde{f}_0+\tilde{f}_\tau\right)}\right)^2}}. \tag{27}$$

Inserting (26) and (27) into (24), we can get the expression of the signal phase after azimuth fast Fourier transform (FFT) as

$$\begin{aligned}\Phi_{2df} = {} & \frac{4\pi}{c}\left(\tilde{f}_0+\tilde{f}_\tau\right)\frac{r_p}{\sqrt{1-\left(\frac{cf_a}{2v\left(\tilde{f}_0+\tilde{f}_\tau\right)}\right)^2}} \\ & -2\pi f_a\left[\frac{x_p}{v}+\frac{r_p\cdot f_a\cdot c}{2v^2\sqrt{\left(\tilde{f}_0+\tilde{t_\tau}\right)^2-\left(\frac{cf_a}{2v}\right)^2}}\right] \\ & +2\pi f_a t-2\pi\tilde{f}_\tau\Delta t. \end{aligned} \tag{28}$$

2) Reference Function Multiplication: The second step of the RMA is bulk focusing through reference function multiplication, after which, under ideal conditions, targets at the reference range can achieve complete focusing, while targets elsewhere can only be partially focused.

The reference function is given by

$$\Phi_{\mathrm{ref}}=-\frac{4\pi}{c}R_{\mathrm{ref}}\sqrt{\left(f_0+f_\tau\right)^2-\left(\frac{cf_a}{2v}\right)^2}-2\pi f_a t. \tag{29}$$

Note that f_0 and f_τ are both ideal frequency. The last term in (29) is to compensate for the additional phase induced by the motion within the sweep.

After reference function multiplication, the signal phase turns into

$$\Phi_{\text{RFM}} = \frac{4\pi}{c}\left(\tilde{f}_0+\tilde{f}_\tau\right)\frac{r_p}{\sqrt{1-\left(\frac{cf_a}{2v\left(\tilde{f}_0+\tilde{f}_\tau\right)}\right)^2}} - 2\pi f_a\left[\frac{x_p}{v}+\frac{r_p\cdot f_a\cdot c}{2v^2\sqrt{\left(\tilde{f}_0+\tilde{f}_\tau\right)^2-\left(\frac{cf_a}{2v}\right)^2}}\right] - \frac{4\pi}{c}R_{\text{ref}}\sqrt{(f_0+f_\tau)^2-\left(\frac{cf_a}{2v}\right)^2} - 2\pi\tilde{f}_\tau\Delta t. \tag{30}$$

3) Stolt Interpolation: Stolt interpolation is the third step of the RMA. It is aimed to realize differential focusing, which means that, under ideal conditions, in this step, residual RCM correction, range–azimuth decoupling, and residual azimuth compression can be all completed simultaneously.

It can be seen as a mapping of variables

$$f_0+f'_\tau = \sqrt{(f_0+f_\tau)^2-\left(\frac{cf_a}{2v}\right)^2} \tag{31}$$

where f'_τ is the new range frequency.

With (19), (21), and (31), we have

$$\begin{aligned}\tilde{f}_0+\tilde{f}_\tau &= f_0-\Delta f_0+\left(1+\frac{\delta k}{k_r}\right)f_\tau \\ &= \left(1+\frac{\delta k}{k_r}\right)(f_0+f_\tau)-\frac{\delta k}{k_r}f_0-\Delta f_0 \\ &= \left(1+\frac{\delta k}{k_r}\right)\sqrt{(f_0+f'_\tau)^2+\left(\frac{cf_a}{2v}\right)^2}-\frac{\delta k}{k_r}f_0-\Delta f_0.\end{aligned} \tag{32}$$

Inserting (31) and (32) into (30), we can get the 2-D spectrum of the target located at (r_p, x_p) after Stolt interpolation as (33), which is shown at the bottom of this page. The ideal 2-D spectrum is

$$\Phi_{\text{ideal}} = \frac{4\pi}{c}(r_p-R_{\text{ref}})\cdot(f_0+f'_\tau)-2\pi f_a\frac{x_p}{v}. \tag{34}$$

In order to make subsequent derivations more concise, we define two new variables as follows:

$$\begin{cases} u = \frac{cf_a}{2v(f_0+f'_\tau)} = \frac{K_x}{K_y} \\ m = \frac{\frac{\delta k}{k_r}\cdot f_0+\Delta f_0}{f_0+f'_\tau} = \frac{\frac{\delta k}{k_r}\cdot K_{yc}+\Delta K_{yc}}{K_y} \end{cases} \tag{35}$$

where $K_x = 2\pi f_a/v$ and $K_y = 4\pi(f_0+f'_\tau)/c$ are the azimuth and range spatial frequency, respectively, also known as wavenumber. $K_{yc} = 4\pi f_0/c$ corresponds to the wavenumber of the carrier frequency. $\Delta K_{yc} = 4\pi\Delta f_0/c$ represents the offset of range center wavenumber.

According to (33)–(35), we can simplify the 2-D phase error as follows:

$$\begin{aligned}\Phi_e &= \Phi_{\text{Stolt}}-\Phi_{\text{ideal}} \\ &= K_y\cdot\left\{r_p\left[\sqrt{\left(\left(1+\frac{\delta k}{k_r}\right)\sqrt{1+u^2}-m\right)^2-u^2}-1\right]-\left[\left(1+\frac{\delta k}{k_r}\right)\sqrt{1+u^2}-m\right]\cdot\frac{c\cdot\Delta t}{2}\right\}.\end{aligned} \tag{36}$$

It can be seen that the frequency shift expressed by (19) and (21) is the same for all the targets, while the phase error (36) is related to the targets' minimum slant range r_p, and therefore, the negative impacts induced by systematical errors should be considered in the imaging algorithm.

Then, (36) can be simplified as

$$\Phi_e(K_x,K_y) = K_y\cdot\xi(u,m) \tag{37}$$

where $\xi(\cdot)$ represents a function dependent on variables u and m. Note that here we use $\xi(\cdot)$ to simplify the following discussion

$$\Phi_{Stolt} = \frac{4\pi}{c}\left[\left(1+\frac{\delta k}{k_r}\right)\sqrt{(f_0+f'_\tau)^2+\left(\frac{cf_a}{2v}\right)^2}-\frac{\delta k}{k_r}f_0-\Delta f_0\right]\cdot\left[\sqrt{1-\left(\frac{cf_a}{2v\left[\left(1+\frac{\delta k}{k_r}\right)\sqrt{(f_0+f'_\tau)^2+\left(\frac{cf_a}{2v}\right)^2}-\frac{\delta k}{k_r}f_0-\Delta f_0\right]}\right)^2}\right]^{-1} - \frac{c\cdot\Delta t}{2}\Bigg] - 2\pi f_a\left[\frac{x_p}{v}+\frac{r_p\cdot f_a\cdot c}{2v^2\sqrt{\left[\left(1+\frac{\delta k}{k_r}\right)\sqrt{(f_0+f'_\tau)^2+\left(\frac{cf_a}{2v}\right)^2}-\frac{\delta k}{k_r}f_0-\Delta f_0\right]^2-\left(\frac{cf_a}{2v}\right)^2}}\right] - \frac{4\pi}{c}R_{ref}(f_0+f'_\tau) \tag{33}$$

since the specific expression of it is not of importance, and what matters is only its dependency on u and m.

It should be pointed out that the above derivations are all under the condition that the trajectory is perfectly ideal. In the more general case where the unknown trajectory error exists, we can draw the same conclusion as described in (37) except that the specific expression of $\xi(\cdot)$ changes. The detailed derivations are provided in the Appendix.

III. Analysis of the 2-D Phase Error

A. Structural Property of the Phase Error

In order to explore the structural property of the 2-D phase error, we apply Taylor expansion on (37) at $K_y = K_{yc}$, i.e., $f'_\tau = 0$; then, we get

$$\begin{aligned}\Phi_e(K_x, K_y) = {} & \phi_0(K_x) + \phi_1(K_x)(K_y - K_{yc}) \\ & + \phi_2(K_x)(K_y - K_{yc})^2 \\ & + \phi_3(K_x)(K_y - K_{yc})^3 + \cdots \end{aligned} \tag{38}$$

where ϕ_0 represents the APE, ϕ_1 refers to the residual RCM, and the residual higher order terms of range wavenumber account for range defocus [34], which cannot be neglected under some circumstances, especially when the resolution is ultrahigh. The influence of the systematical errors is reflected in the Taylor coefficients of (38), $\phi_0(K_x)$, $\phi_1(K_x)$, $\phi_2(K_x)$, etc., since these coefficients are dependent on the error term m, which will be shown in detail next.

The analytical expressions of the coefficients in the Taylor series (38) are described as follows:

$$\phi_0(K_x) = K_{yc} \cdot \xi(u_{yc}, m_{yc}) \tag{39}$$

$$\begin{aligned}\phi_1(K_x) = {} & \xi(u_{yc}, m_{yc}) - u_{yc}\left[\frac{\partial}{\partial u}\xi(u,m)\right]\Big|_{K_y=K_{yc}} \\ & - m_{yc}\left[\frac{\partial}{\partial m}\xi(u,m)\right]\Big|_{K_y=K_{yc}}\end{aligned} \tag{40}$$

$$\begin{aligned}\phi_2(K_x) = {} & \frac{1}{2K_{yc}}\left\{ u_{yc}^2\left[\frac{\partial^2}{\partial u^2}\xi(u,m)\right]\Big|_{K_y=K_{yc}}\right. \\ & + m_{yc}^2\left[\frac{\partial^2}{\partial m^2}\xi(u,m)\right]\Big|_{K_y=K_{yc}} \\ & \left. + 2u_{yc}m_{yc}\left[\frac{\partial^2}{\partial u\partial m}\xi(u,m)\right]\Big|_{K_y=K_{yc}}\right\}\end{aligned} \tag{41}$$

$$\begin{aligned}\phi_3(K_x) = {} & -\frac{1}{2K_{yc}^2}\left\{ u_{yc}^2\left[\frac{\partial^2}{\partial u^2}\xi(u,m)\right]\Big|_{K_y=K_{yc}}\right. \\ & + m_{yc}^2\left[\frac{\partial^2}{\partial m^2}\xi(u,m)\right]\Big|_{K_y=K_{yc}} \\ & \left. + 2u_{yc}m_{yc}\left[\frac{\partial^2}{\partial u\partial m}\xi(u,m)\right]\Big|_{K_y=K_{yc}}\right\} \\ & - \frac{1}{6K_{yc}^2}\left\{ u_{yc}^3\left[\frac{\partial^3}{\partial u^3}\xi(u,m)\right]\Big|_{K_y=K_{yc}}\right. \\ & + m_{yc}^3\left[\frac{\partial^3}{\partial m^3}\xi(u,m)\right]\Big|_{K_y=K_{yc}} \\ & + 3u_{yc}^2m_{yc}\left[\frac{\partial^3}{\partial u^2\partial m}\xi(u,m)\right]\Big|_{K_y=K_{yc}} \\ & \left. + 3u_{yc}m_{yc}^2\left[\frac{\partial^3}{\partial u\partial m^2}\xi(u,m)\right]\Big|_{K_y=K_{yc}}\right\}\end{aligned} \tag{42}$$

where

$$\begin{cases} u_{yc} = \frac{cf_a}{2vf_0} = \frac{K_x}{K_{yc}} \\ m_{yc} = \frac{\frac{\delta k}{k_r}\cdot f_0 + \Delta f_0}{f_0} = \frac{\delta k}{k_r} + \frac{\Delta K_{yc}}{K_{yc}} \end{cases}. \tag{43}$$

Note that m_{yc} is an error term dependent on δk and Δf_0 described by (20). Considering the quadratic and cubic terms of m_{yc} in (41) and (42), on the one hand, ϕ_0 and ϕ_1 are both univariate functions of K_x; thus, it is impossible to obtain the quadratic and higher order derivative of $\xi(u,m)$ to m from them; on the other hand, the higher order error terms are generally minor compared with the lower order ones, so it makes sense to ignore those quadratic and cubic terms of m_{yc}.

Hence, we just leave out the quadratic and cubic terms of m_{yc}; then, (41) and (42) can be approximated as

$$\begin{aligned}\phi_2(K_x) \approx {} & \frac{u_{yc}^2}{2K_{yc}}\left[\frac{\partial^2}{\partial u^2}\xi(u,m)\right]\Big|_{K_y=K_{yc}} \\ & + \frac{u_{yc}m_{yc}}{K_{yc}}\left[\frac{\partial^2}{\partial u\partial m}\xi(u,m)\right]\Big|_{K_y=K_{yc}}\end{aligned} \tag{44}$$

$$\begin{aligned}\phi_3(K_x) \approx {} & -\frac{u_{yc}^2}{2K_{yc}^2}\left[\frac{\partial^2}{\partial u^2}\xi(u,m)\right]\Big|_{K_y=K_{yc}} \\ & - \frac{u_{yc}m_{yc}}{K_{yc}^2}\left[\frac{\partial^2}{\partial u\partial m}\xi(u,m)\right]\Big|_{K_y=K_{yc}} \\ & - \frac{u_{yc}^3}{6K_{yc}^2}\left[\frac{\partial^3}{\partial u^3}\xi(u,m)\right]\Big|_{K_y=K_{yc}} \\ & - \frac{u_{yc}^2m_{yc}}{2K_{yc}^2}\left[\frac{\partial^3}{\partial u^2\partial m}\xi(u,m)\right]\Big|_{K_y=K_{yc}}\end{aligned} \tag{45}$$

According to (39), (40), (44), and (45), we can get the analytical relationship among them as follows:

$$\phi_2(K_x) \approx -\frac{K_x}{K_{yc}}\frac{d\phi_1(K_x)}{dK_x} - \frac{K_x^2}{2K_{yc}^2}\frac{d^2\phi_0(K_x)}{dK_x^2} \tag{46}$$

and

$$\begin{aligned}\phi_3(K_x) \approx {} & \frac{K_x}{K_{yc}^2}\frac{d\phi_1(K_x)}{dK_x} + \frac{K_x^2}{2K_{yc}^2}\frac{d^2\phi_1(K_x)}{dK_x^2} \\ & + \frac{K_x^2}{K_{yc}^3}\frac{d^2\phi_0(K_x)}{dK_x^2} + \frac{K_x^3}{3K_{yc}^3}\frac{d^3\phi_0(K_x)}{dK_x^3}.\end{aligned} \tag{47}$$

B. Influence on Range Defocus

Compared to relatively low-resolution situations, range defocus is more notable for ultrahigh-resolution SAR. In this part, we will analyze the effects of the above systematical errors on range defocus, which are related to the quadratic and higher order terms of range wavenumber in (38). For the simplicity of analysis, we only consider the quadratic-order term, i.e., $\phi_2(K_x)$ in this part, which can show the influence on focusing quality intuitively.

Through simulations, we find that APE and RCM caused by those errors mentioned previously both exhibit an approximate quadratic relationship concerning K_x, which will be validated later in the simulation section. Therefore, it makes sense to suppose that APE and RCM contain only quadratic terms, that is

$$\begin{cases} \phi_0(K_x) = p_0 K_x^2 \\ \phi_1(K_x) = p_1 K_x^2 \end{cases}. \tag{48}$$

Inserting (48) into (46), we can get

$$\phi_2(K_a) = -\left(2p_1 K_{yc} + p_0\right) \frac{K_x^2}{K_{yc}^2}. \tag{49}$$

Then, the quadratic term of the 2-D phase error can be expressed as

$$\phi_2(K_a)\left(K_y - K_{yc}\right)^2 = -\left(2p_1 K_{yc} + p_0\right) \frac{K_x^2}{K_{yc}^2}\left(K_y - K_{yc}\right)^2. \tag{50}$$

Use ρ_x and ρ_y to represent the azimuth and range resolution cells, respectively. Then, the limits of azimuth and range wavenumber can be expressed as

$$\begin{cases} K_x \in \left[-\frac{\pi}{\rho_x}, +\frac{\pi}{\rho_x}\right] \\ K_y - K_{yc} \in \left[-\frac{\pi}{\rho_y}, +\frac{\pi}{\rho_y}\right] \end{cases}. \tag{51}$$

Generally, when the phase error exceeds $\pi/4$, it is considered that there will be non-negligible defocus. Therefore, if range defocus exists, that means

$$\begin{aligned} &\max\left\{\phi_2(K_x)\left(K_y - K_{yc}\right)^2\right\} \\ &-\min\left\{\phi_2(K_x)\left(K_y - K_{yc}\right)^2\right\} > \frac{\pi}{4}. \end{aligned} \tag{52}$$

Inserting (50) and (51) into (52), then the restriction where range defocus is non-negligible can be expressed as

$$\left|\frac{8\pi}{\lambda} p_1 + p_0\right| > \frac{4\rho_x^2 \rho_y^2}{\pi \lambda^2}. \tag{53}$$

Considering only the quadratic-order term, if (53) holds, it means that conventional residual RCM and APE correction is unable to meet the requirements of focusing quality, and it is necessary to carry out 2-D autofocus.

C. Space-Variant Property of the Phase Error

According to (36), under the condition where the trajectory of the radar platform is perfectly ideal, the 2-D phase error is a linear function of the minimum slant range r_p. Besides, there is no relationship between the 2-D phase error and the azimuth position of targets, x_p.

ϕ_0 and ϕ_1 are the zeroth and first derivatives of the 2-D phase error at $K_y = K_{yc}$, respectively. Therefore, ϕ_0 and ϕ_1 are obviously both linear functions of r_p, too. Then, according to (46) and (47), ϕ_2 and ϕ_3 are also linearly dependent on slant range. Furthermore, they are all independent of the azimuth position of targets.

Hence, based on the above analysis, we can draw the conclusion that if the slant range error is ignorable after motion compensation, the APE, residual RCM, and the higher order error of range wavenumber, ϕ_2 and ϕ_3, which are caused by the systematical errors, are all linearly related to the range position of targets and, in the meantime, are all azimuth invariant.

TABLE I
MAIN PARAMETERS FOR PROCESSING

Parameters	Values
Carrier frequency	15.14 GHz
Bandwidth	5.72GHz
Sampling frequency	2500 MHz
Time width	99.5 us
Nominal flight Height	578.6 m
Azimuth Bandwidth	2800 Hz
Pulse repetition frequency	5000 Hz
Nominal Velocity	67 m/s

IV. PROPOSED METHOD

As mentioned earlier, in the case where conventional 1-D autofocus methods cannot meet the requirements of focusing quality, it is obliged to carry out 2-D autofocus.

In Section III-A, we have performed a detailed analysis of the structural property of the 2-D phase error. The analytical relationships among the coefficients of Taylor series of 2-D phase error $\phi_0(K_x)$, $\phi_1(K_x)$, $\phi_2(K_x)$, and $\phi_3(K_x)$ are shown in (46) and (47). Therefore, it is straightforward to obtain the estimations, $\hat{\phi}_2(K_x)$ and $\hat{\phi}_3(K_x)$, as long as $\hat{\phi}_0(K_x)$ and $\hat{\phi}_1(K_x)$ are known, which can be easily estimated by conventional 1-D autofocus methods. In this section, we will describe the processing steps of the proposed 2-D autofocus method in detail.

A. Prominent Scatter Selection

As discussed in Section III-C, the phase error terms that we want to compensate for are all linear related to the slant range, so in order to compensate for the range-variant phase error accurately, we need to carry out different compensation for targets located in different range positions. Therefore, the first step of the proposed method is to select prominent scatters located in different positions, so that we can perform linear fitting along the slant range and conduct range-dependent compensation subsequently. To ensure a reliable estimation result as far as possible, we can use one of the following criteria to select prominent scatters: 1) scatters of which the peak value of the main lobe is much higher than the background noise; and 2) scatters that have a higher signal-to-noise ratio. Besides, to improve the estimation accuracy, we had better choose scatters

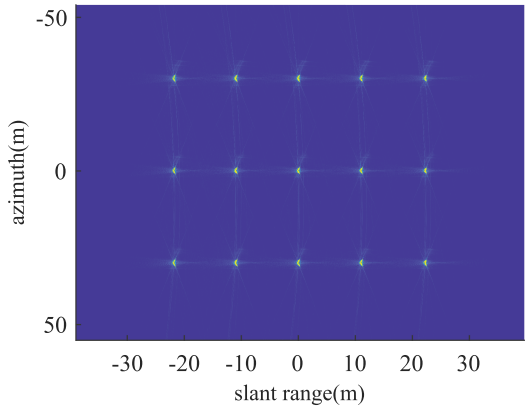

Fig. 6. Original coarse focused image processed by the RMA with MOCO.

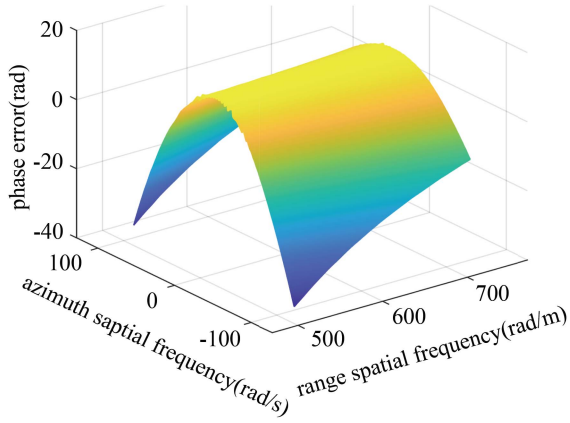

Fig. 7. 2-D phase error surface of point 8.

distributed in different range positions as wide as possible. If there are no prominent scatters, small regions that contain strong scattering characteristics can also be alternatives.

B. Residual RCM Estimation

The absence of residual RCM is a prerequisite for an accurate estimation of APE; thus, range alignment must be performed to remove the residual RCM prior to APE estimation and correction.

Range alignment methods based on image evaluation functions can achieve high alignment accuracy, but they are computationally intensive and time consuming. Since we only perform range alignment for the small blocks of the selected prominent scatters, the amount of processed data is small, so those methods based on image evaluation functions are good choices to obtain high-precision envelope alignment results. In this article, we adopt the global minimum entropy method [22] to estimate the residual RCM.

C. APE Estimation

After residual RCM estimation and correction, the next step is to execute APE estimation, which can be complemented by conventional 1-D autofocus methods such as PGA [28], MDA [25], [37], etc. Since the dominant component of APE is the quadratic term, we choose MDA as the APE estimation method in this article.

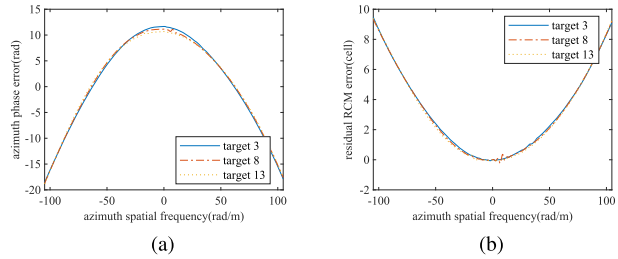

Fig. 8. APE and residual RCM of targets 3, 8, and 13 of the original image processed by the RMA. (a) APEs of three targets. (b) Residual RCMs of three targets.

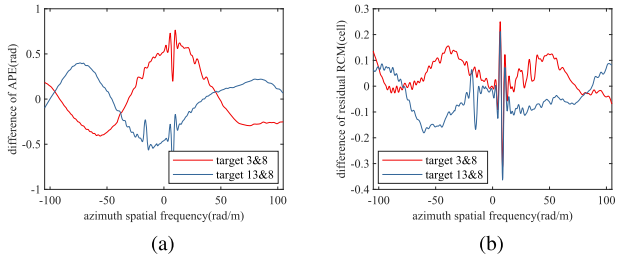

Fig. 9. Difference of APE and residual RCM between targets 3 and 8 and targets 8 and 13. (a) Difference of APE. (b) Difference of residual RCMs.

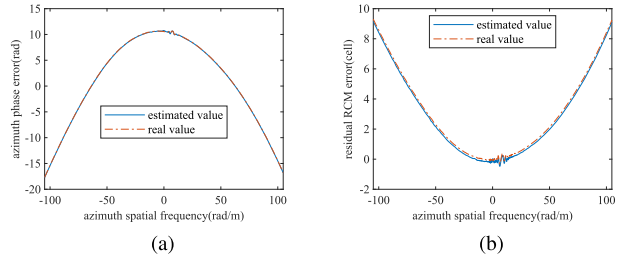

Fig. 10. Estimated and real value of APE and residual RCM of target 10. (a) APE. (b) Residual RCM.

D. Linear Fitting Along Slant Range

By now, we have obtained the estimations of residual RCM $\hat{\phi}_1(K_x)$ and APE $\hat{\phi}_0(K_x)$ of the selected prominent blocks. Then, the next step is to fit $\hat{\phi}_0(K_x)$ and $\hat{\phi}_1(K_x)$ along the slant range.

Suppose that the estimated APE and residual RCM (considering only the dominant components, the quadratic terms) of those blocks are expressed as

$$\begin{cases} \hat{\phi}_{0,i}(K_x) & = A_{0,i}K_x^2 \\ \hat{\phi}_{1,i}(K_x) & = A_{1,i}K_x^2 + B_{1,i}K_x \end{cases}, \quad i = 1, 2, \ldots, n \tag{54}$$

where the subscript i represents the estimations of the ith prominent scatter region, and n represents the number of those regions. $A_{0,i}$ and $A_{1,i}$ are both the second-order fitting coefficients, and

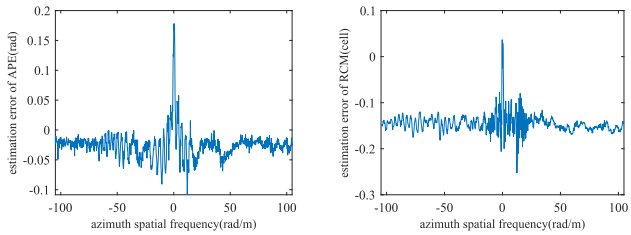

Fig. 11. Estimation error of linear fitting along slant range of target 10. (a) APE. (b) Residual RCM.

$B_{1,i}$ is the first-order fitting coefficient of $\hat{\phi}_{1,i}(K_x)$. Since the linear term of APE corresponds to an undesirable azimuth offset of the image, it will be generally removed before correction. Besides, we adopt MDA as the APE estimation algorithm, which is only capable of the estimation of the quadratic order of phase error. Therefore, $\hat{\phi}_{0,i}(K_x)$ contains only the quadratic term.

After linear fitting, we can get

$$\begin{cases} A_{0,i} &= \alpha_0 \cdot r_i + \beta_0 \\ A_{1,i} &= \alpha_1 \cdot r_i + \beta_1 \\ B_{1,i} &= \alpha_2 \cdot r_i + \beta_2 \end{cases}, \quad i = 1, 2, \ldots, n \tag{55}$$

where r_i is the range position of the ith prominent scatter, and α_j and β_j $(j = 0, 1, 2)$ are the linear coefficients and constant terms of linear fitting, respectively.

Then, the estimated values of targets located at an arbitrary range coordinate r are

$$\begin{cases} \hat{\phi}_0(K_x, r) &= (\alpha_0 \cdot r + \beta_0) K_x^2 \\ \hat{\phi}_1(K_x, r) &= (\alpha_1 \cdot r + \beta_1) K_x^2 + (\alpha_2 \cdot r + \beta_2) K_x \end{cases}. \tag{56}$$

Inserting (56) into (46) and (47), respectively, we can get the corresponding estimations as follows:

$$\begin{cases} \hat{\phi}_2(K_x, r) \approx & -\frac{K_x}{K_{yc}} \left(2 (\alpha_1 \cdot r + \beta_1) K_x + \alpha_2 \cdot r + \beta_2\right) \\ & -\frac{K_x^2}{K_{yc}^2} (\alpha_0 \cdot r + \beta_0) \\ \hat{\phi}_3(K_x, r) \approx & \frac{K_x}{K_{yc}^2} \left(2 (\alpha_1 \cdot r + \beta_1) K_x + \alpha_2 \cdot r + \beta_2\right) \\ & + \frac{K_x^2}{K_{yc}^2} (\alpha_1 \cdot r + \beta_1) + \frac{2K_x^2}{K_{yc}^3} (\alpha_0 \cdot r + \beta_0) \end{cases}. \tag{57}$$

For simplicity, (56) and (57) can be uniformly written as

$$\hat{\phi}_i(K_x, r) = \kappa_i(K_x) \cdot r + \nu_i(K_x), \quad i = 0, 1, 2, 3 \tag{58}$$

where $\kappa_i(K_x)$ and $\nu_i(K_x)$ are the linear coefficient of range r and the range independent offset, respectively.

E. Range Blocking

In order to compensate for the phase error in the 2-D spatial frequency domain, in the consideration of the space-variant property of the error, it is a usual practice to split the whole image into small blocks. As the phase error we discussed is only range variant, we just need to split the image along the range dimension.

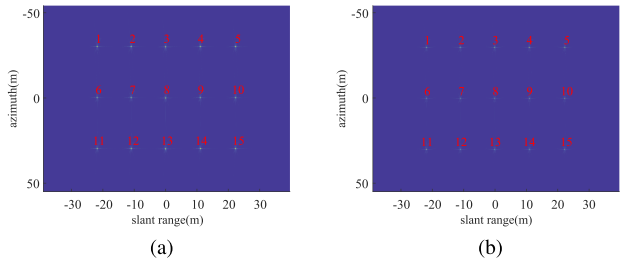

Fig. 12. Refocused image processed by (a) the PGA and (b) the proposed method.

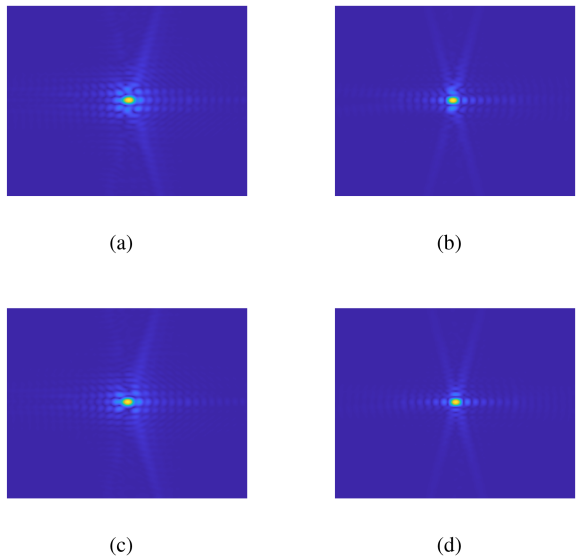

Fig. 13. Enlarged local area of point 1 processed by (a) the PGA and (b) the proposed method and point 8 processed by (c) the PGA and (d) the proposed method.

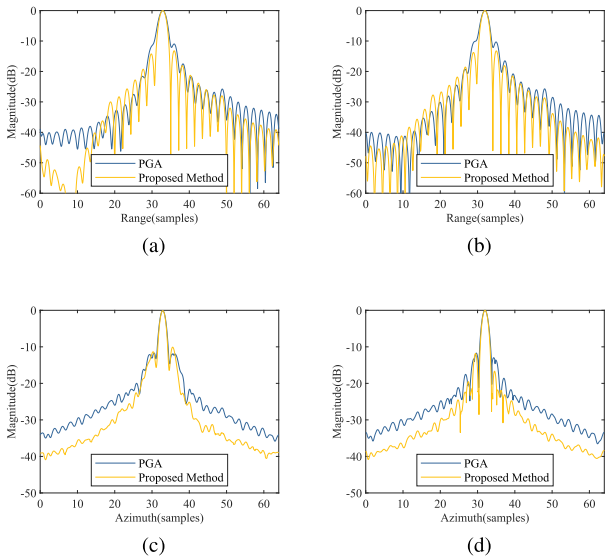

Fig. 14. (a) and (b) Range profiles of points 1 and 8, respectively. (c) and (d) Azimuth profiles of points 1 and 8, respectively.

TABLE II
INDEX MEASUREMENT RESULTS OF THE SIMULATED DATA

			5	8	11
PGA	Range	IRW (m)	0.029	0.028	0.027
		PSLR (dB)	−10.686	−10.313	−9.081
		ISLR (dB)	−10.965	−10.382	−7.008
	Azimuth	IRW (m)	0.022	0.022	0.022
		PSLR (dB)	−11.351	−11.709	−10.166
		ISLR (dB)	−6.281	−7.469	−5.958
Proposed Method	Range	IRW (m)	0.026	0.025	0.025
		PSLR (dB)	−13.246	−13.248	−13.057
		ISLR (dB)	−10.947	−10.756	−10.515
	Azimuth	IRW (m)	0.020	0.021	0.021
		PSLR (dB)	−11.888	−11.818	−10.125
		ISLR (dB)	−8.832	−12.014	−8.212

TABLE III
IMAGE QUALITY INDEX OF THE SIMULATED DATA

	Original	PGA	Proposed Method
Entropy	9.6015	7.0162	6.1503
Contrast	11.8662	13.8891	14.7429

TABLE IV
INDEX MEASUREMENT RESULTS OF TARGETS IN THE REAL-DATA EXPERIMENT

			PGA	Proposed Method
Target A	Range	IRW (m)	0.0265	0.0257
		PSLR (dB)	-7.601	-12.350
		ISLR (dB)	-6.235	-8.448
	Azimuth	IRW (m)	0.0343	0.0292
		PSLR (dB)	-19.105	-18.398
		ISLR (dB)	-16.655	-16.490
Target B	Range	IRW (m)	0.0263	0.0255
		PSLR (dB)	-7.098	-12.178
		ISLR (dB)	-5.382	-7.500
	Azimuth	IRW (m)	0.0346	0.0297
		PSLR (dB)	-16.702	-20.380
		ISLR (dB)	-15.021	-15.320

TABLE V
IMAGE QUALITY INDEX OF THE REAL-DATA EXPERIMENT

	Original	PGA	Proposed Method
Entropy	15.0575	14.7350	14.6292
Contrast	1.0966	1.1185	1.1355

As for the size of each block, in order to make the error difference within each block negligible, we choose $\pi/4$ as the limit of the differences of APEs and range defocus terms, and half a range gate as the limit of RCM.

Here, for simplicity, we just consider the quadratic range defocus term; then, the restrictions can be expressed as

$$\max\left\{\Delta\hat{\phi}_0\right\} = \max|\kappa_0(K_x)|\cdot\Delta r < \frac{\pi}{4} \tag{59a}$$

$$\max\left\{\Delta\hat{\phi}_1\right\} = \max|\kappa_1(K_x)|\cdot\Delta r < \frac{rgate}{2} \tag{59b}$$

$$\begin{aligned}&\max\left\{\Delta\hat{\phi}_2\left(K_y-K_{yc}\right)^2\right\}\\ &=\max\left\{|\kappa_2(K_x)|\left(K_y-K_{yc}\right)^2\right\}\cdot\Delta r<\frac{\pi}{4}\end{aligned} \tag{59c}$$

where Δr is the width of each block and $rgate$ is the size of a range gate.

Consider that during the mapping from $\hat{\phi}_0$ and $\hat{\phi}_1$ to $\hat{\phi}_2$ and $\hat{\phi}_3$, new RCM and APE may be introduced due to estimation errors. Therefore, we can only consider the inequality (59c) and leave the difference of original $\hat{\phi}_0$ and $\hat{\phi}_1$ within each block to be compensated together with the introduced new ones later.

Then, according to (59c), the size of range blocks needs to satisfy

$$\Delta r < \frac{\rho_y^2}{4\pi}\cdot\frac{1}{\max|\kappa_2(K_x)|}. \tag{60}$$

F. 2-D Phase Compensation

After range blocking, we can compensate for the 2-D phase error within each block uniformly according to (56) and (57), by setting r to the center range of each block.

G. Residual RCM and APE Compensation

After 2-D phase compensation, there are still original residual RCM and APE that have not been compensated for due to their spatial-variant property. Besides, there are also new RCM and APE introduced during the estimation process. Therefore, it is necessary to perform residual RCM and APE compensation again. Fortunately, since the main higher order error of range wavenumber has been compensated for, we can deal with the residual RCM and APE by conventional 1-D autofocus methods.

The whole flowchart of the proposed method is shown in Fig. 3. It should be pointed out that the APE and RCM estimation methods that we choose here are not unique and can be replaced by others. What matters in the proposed method is the selection of the range block size and the mapping relationship described by (46) and (47).

V. EXPERIMENTAL RESULTS

To verify the correctness of the theoretical analysis and the effectiveness of the proposed method, simulations and real data experiments are conducted. Both the simulation and real data used in this article are based on the MWP SAR system described in [38].

A. Simulation Results

The simulation parameters are taken from an MWP FMCW SAR system developed by the Aerospace Information Research Institute, Chinese Academy of Sciences, which is shown in Table I. The trajectory used for simulation is taken from a segment of a real fight history of the system. Fig. 4 shows the trajectory deviation of the radar platform. In addition to the error introduced by trajectory deviation, we set the systematical errors as follows: the synchronization error during signal mixing δt_1 and δt_2 are set to 0.0267 and 0.0067 μs, respectively, which

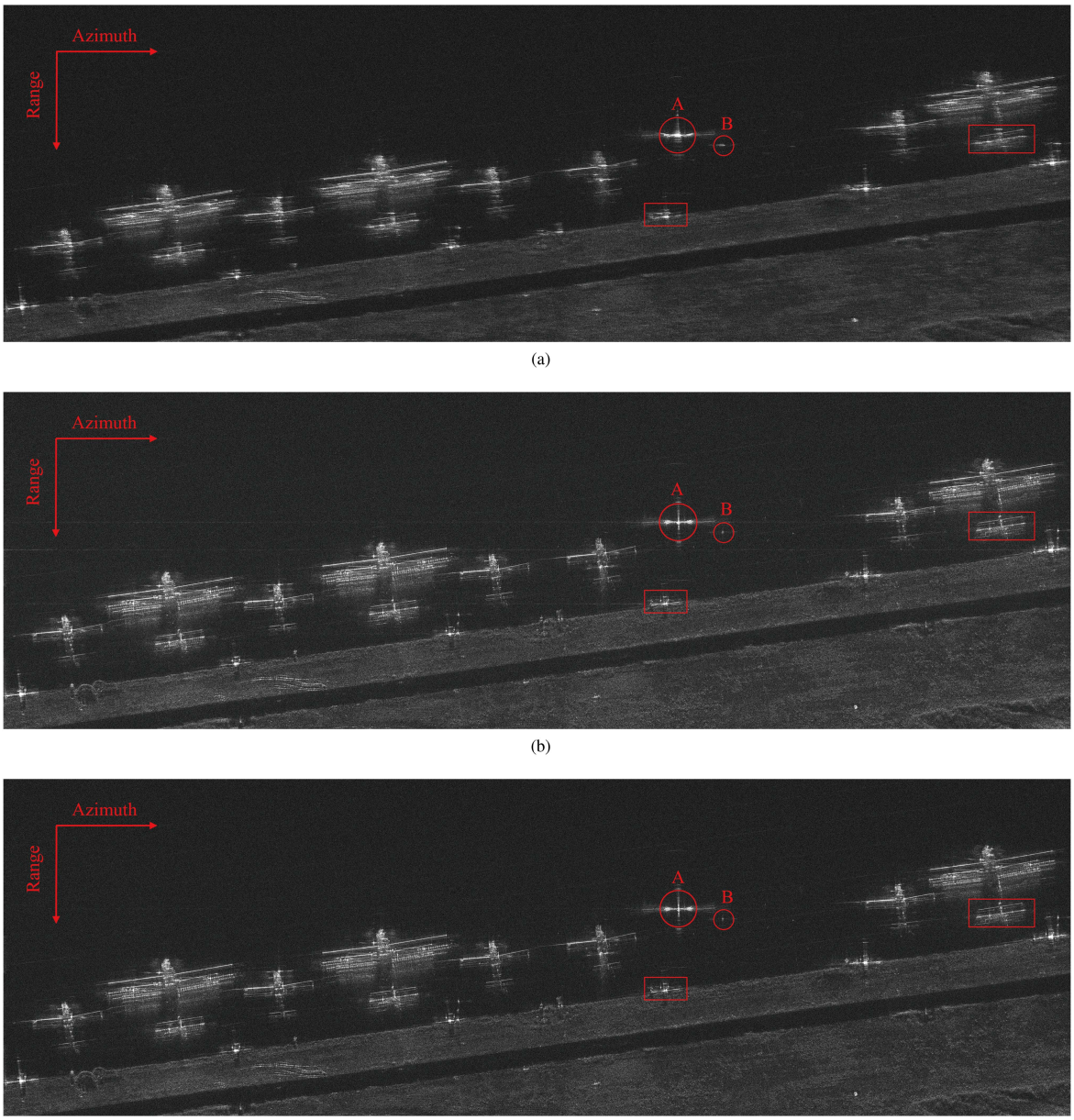

Fig. 15. Results of (a) the original image processed by the RMA, (b) the refocused image processed by the PGA, and (c) the refocused image processed by the proposed method.

correspond to the slant range of 4 and 1 m; the unknown system delay error δt_3 is set to 0.0400 μs, which corresponds to the slant range of 6 m; and the ratio of the FM rate error δk and the ideal one k_r is set to 0.0077.

We set a scenario that contains 15 points, which is shown in Fig. 5. The size of the scenario is set to about 100 m (Azimuth)×80 m (Range), and the point number of the simulated data is 8192×6000, which is comparable to the scene size of the real data that will be presented later. Choosing RMA as the processing algorithm, combined with direct MOCO algorithm (DMA) [39], the simulated echo is processed to get the original coarse focused image, as shown in Fig. 6.

First, we choose points 3, 8, and 13 in Fig. 5 to verify the azimuth space-invariant property of the 2-D phase error. Comparing the 2-D phase of the coarse focused image with the ideal one, we can get the phase error of these three points. In order to get an overall understanding of the 2-D error, we show the phase error surface of point 8 in the 2-D spatial frequency domain in Fig. 7. The APE ϕ_0 and residual RCM ϕ_1 of the three points are shown in Fig. 8, which both show parabolic shapes, as stated in Section III-B. To be more intuitive, we show the error difference of ϕ_0 and ϕ_1 between targets 3 and 8 and targets 8 and 13 in Fig. 9. Note that the APE and residual RCM are induced not only by the inaccurate imaging parameters, but also by residual motion error after motion compensation, which is actually space variant. Even so, from Fig. 9, the maximum value of the difference of APE is about 0.76, which is still smaller than $\pi/4$, and the difference of residual RCM is smaller than half a

range gate. Therefore, with the assistance of relatively accurate navigation data from motion sensors, the phase error caused by inaccurate imaging parameters can be regarded as azimuth invariant.

Second, we choose points 6–10 in Fig. 5 to verify the linear relationship between the 2-D phase error and the slant range. As before, we can get the phase error of these five points by comparing the 2-D phase of the coarse focused image with the ideal one. Next, linear fitting is performed using ϕ_0 and ϕ_1 of targets 6–9, after which we can get the estimated $\hat{\phi}_0$ and $\hat{\phi}_1$ of targets 10, which is shown in Fig. 10. Fig. 11 shows the difference between the estimated value and the real one. Through the above results, it can be proved that the conclusion of the linear relationship between 2-D phase error and slant range holds.

Finally, to better demonstrate the superiority of the proposed method over the conventional 1-D autofocus method, PGA, in the compensation for systematical errors, the original coarse focused image is postprocessed by both the two algorithms, and the results are shown in Fig. 12. And the local region of points 1 and 8 in the two results are enlarged and shown in Fig. 13. Fig. 14 shows the range and azimuth profiles of points 1 and 8 processed by the PGA and the proposed method. The results represented by the above figures can show the superiority of the proposed method intuitively. To show the effectiveness of the proposed method quantitatively, Table II represents some image quality indexes of targets 5, 8, and 11 after being processed by the PGA and the proposed method, including impulse response width (IRW), peak sidelobe ratio (PSLR), and integral sidelobe ratio (ISLR). Besides, we also measured the entropy and contrast of the original image and the results of PGA and the proposed method, which are shown in Table III. These measurement indexes verify the effectiveness of the proposed method.

B. Real Data Results

To validate the effectiveness of the proposed 2-D autofocus method, the real data acquired from the Ku-band MWP FMCW SAR system mentioned in Section V-A are processed. The main parameters are exactly the same as shown in Table I. The size of the scenario is about 147 m (Azimuth)×46 m (Range), and the point number of the real data is 11 090×3500.

As the simulation part, the real data are also first processed by the RMA combined with DMA to get the original coarse focused image, as shown in Fig. 15(a). Then, the coarse focused image is postprocessed by both the PGA and the proposed method, and the results are shown in Fig. 15(b) and 15(c). To show the results more clearly, the local areas within the boxes in Fig. 15 are enlarged, which are shown in Fig. 16.

Circles A and B in Fig. 15 identify a reflector and a point-like target, respectively. We conduct a detailed analysis of the two targets. Fig. 17 shows the results of range–Doppler domain of the regions within circles A and B in Fig. 15(a)–(c), respectively. The subimages in the left column of Fig. 17 are the results of the reflector A, and subimages in the right column are the results of the point-like target B. In Fig. 17, we can see that in the image processed by the PGA, there still exists visible range defocus, especially on both ends of the azimuth frequency, while this phenomenon is obviously alleviated in the image processed by the proposed method. Fig. 18 represents the contour images of targets A and B after 16 times interpolation. The range and azimuth profiles of the two targets of the original and processed images are shown in Fig. 19. The above results can show the superiority of the proposed method intuitively.

To compare the proposed method and the conventional method quantitatively, we represent the image quality indexes of targets A and B in Table IV. Owing to azimuth windowing

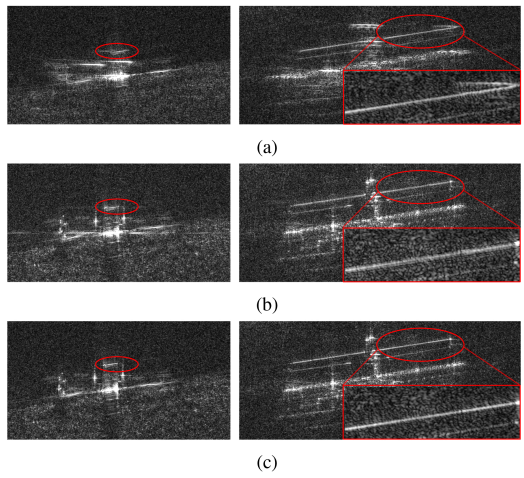

Fig. 16. (a) Enlarged local area of the original coarse focused image. (b) Enlarged local area of the image processed by the PGA. (c) Enlarged local area of the image processed by the proposed method.

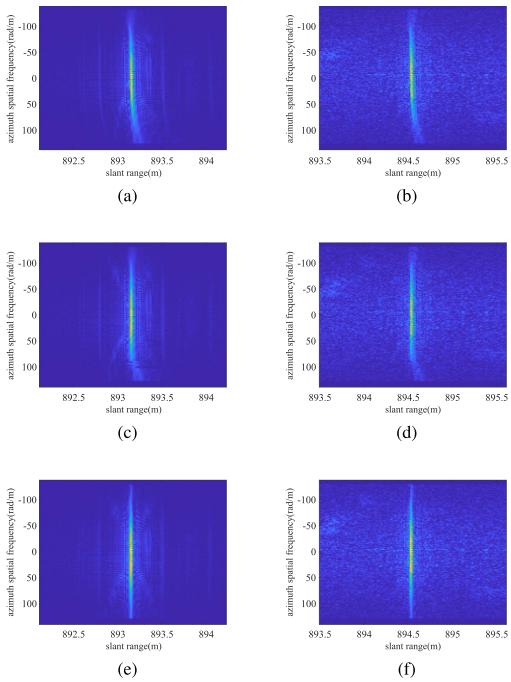

Fig. 17. Results of range–Doppler domain of targets A and B. The left-column subimages correspond to the results of reflector A, and the right-column subimages correspond to the results of the point-like target B. (a) and (b) Range–Doppler domain of the original image. (c) and (d) Range–Doppler domain of the image processed by the PGA. (e) and (f) Range–Doppler domain of the image processed by the proposed method.

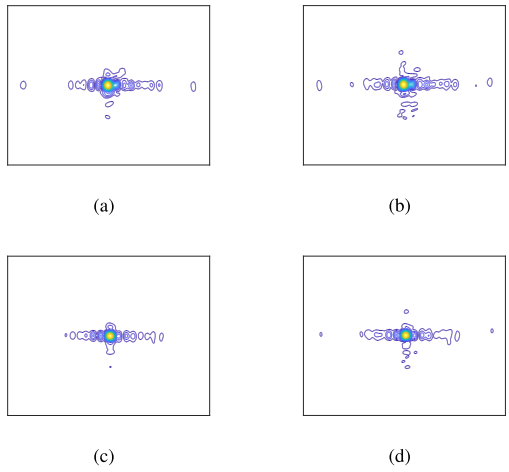

Fig. 18. Contour images of targets A and B after 16 times interpolation. Results of (a) target A and (b) target B processed by the PGA. Results of (c) target A and (d) target B processed by the proposed method.

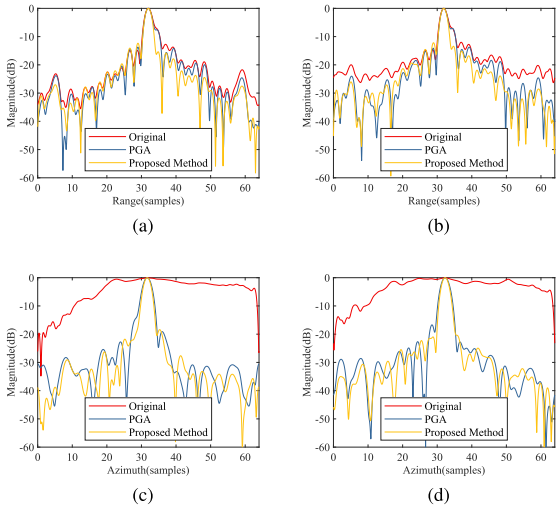

Fig. 19. Range profiles of (a) target A and (b) target B. Azimuth profiles of (c) target A and (d) target B.

during the imaging process, the PSLR and ISLR in the azimuth are lower than that in the range. The image entropy and contrast are also measured and listed in Table V. It can be seen that our method acquires a lower entropy and higher contrast than those of PGA, which validates the effectiveness of the proposed method. As for the efficiency, it depends on the size and number of the selected prominent scatter regions. In this real data experiment, we select six such regions distributed in different range positions, and each of them is 256 (points) $\times$ 256 (points), and the time consumed by the proposed method is just about 5% longer than the traditional PGA.

VI. Conclusion

In this article, we analyzed the impact of three sources of possible errors, i.e., synchronization error between the transmit channel and the mixing channel, unknown system delay during signal reception, and inaccurate FM rate of the UWB signal on MWP SAR images processed by the RMA. For MWP SAR images that have ultrahigh resolution, these systematical errors mentioned before will cause degradation in the final image. Therefore, concerning these unknown systematical errors, it is obliged to propose a new method to compensate for them.

First, we established the signal model in the presence of the three kinds of systematical errors and obtained the 2-D phase error of the coarse focused image processed by the RMA. Then, we analyzed the structural and space-variant properties of the phase error. Based on the analytical structure, and taking into account the space-variant property, we proposed a new 2-D autofocus method, in which we compensated not only APE and residual RCM, but also high-order terms of range frequency, so that range defocus can be significantly improved. Finally, to validate the effectiveness of the proposed method, both simulated and real data were processed, and the results showed the superior performance of the new method.

Appendix

To get the 2-D phase error in the case where unknown trajectory deviation exists, we need to follow the same deduction process as in Section II-C, except that $\Delta R \neq 0$. Then, the round-trip time is given by

$$t_p = \frac{2}{c}\left[\sqrt{r_p^2 + (v\eta + vt - x_p)^2} + \Delta R\left(t, \eta\right)\right]. \tag{61}$$

The first step is to perform azimuth FT to the dechirped signal, which is the same as (24). Inserting (61) into (25), we can get the SP point as follows:

$$\eta^* = \vartheta\left(\frac{f_a}{\tilde{f}_0 + \tilde{f}_\tau}\right) - t \tag{62}$$

where $\vartheta(\cdot)$ is a function that represents the relationship between η^* and f_a. Since the exact expression of $\Delta R(t, \eta)$ cannot be obtained, there is no way to get the specific expression of $\vartheta(\cdot)$. Fortunately, it does not affect the subsequent derivation.

Inserting (62) into (24), the phase after azimuth FT can be written as

$$\begin{aligned}\Phi_{2df} &= \frac{4\pi}{c}\left(\tilde{f}_0 + \tilde{f}_\tau\right)\cdot R\left(\eta^*\right) - 2\pi f_a \eta^* - 2\pi \tilde{f}_\tau \Delta t \\ &= \frac{4\pi}{c}\left(\tilde{f}_0 + \tilde{f}_\tau\right)\cdot \zeta\left(\frac{f_a}{\tilde{f}_0 + \tilde{f}_\tau}\right) - 2\pi f_a \cdot \vartheta\left(\frac{f_a}{\tilde{f}_0 + \tilde{f}_\tau}\right) \\ &\quad + 2\pi f_a t - 2\pi \tilde{f}_\tau \Delta t\end{aligned} \tag{63}$$

where $\zeta(\cdot)$ represents the instantaneous range at the SP point.

The second step is reference function multiplication. Multiplying (63) with the matched filter (29), we can get

$$\begin{aligned}\Phi_{\text{RFM}} &= \frac{4\pi}{c}\left(\tilde{f}_0 + \tilde{f}_\tau\right)\cdot \zeta\left(\frac{f_a}{\tilde{f}_0 + \tilde{f}_\tau}\right) - 2\pi f_a \vartheta\left(\frac{f_a}{\tilde{f}_0 + \tilde{f}_\tau}\right) \\ &\quad - \frac{4\pi}{c} R_{\text{ref}} \sqrt{(f_0 + f_\tau)^2 - \left(\frac{c f_a}{2v}\right)^2} - 2\pi \tilde{f}_\tau \Delta t.\end{aligned} \tag{64}$$

The third step is Stolt interpolation realized by variable substitution. Then, the expression of phase becomes (65) shown at the top of the next page.

$$\Phi_{\text{Stolt}} = \frac{4\pi}{c}\left[\left(1+\frac{\delta k}{k_r}\right)\sqrt{(f_0+f_\tau')^2+\left(\frac{cf_a}{2v}\right)^2}-\frac{\delta k}{k_r}f_0-\Delta f_0\right]\cdot\left[\zeta\left(\frac{f_a}{\left(1+\frac{\delta k}{k_r}\right)\sqrt{(f_0+f_\tau')^2+\left(\frac{cf_a}{2v}\right)^2}-\frac{\delta k}{k_r}f_0-\Delta f_0}\right)-\frac{c\cdot\Delta t}{2}\right]-2\pi f_a\vartheta\left(\frac{f_a}{\left(1+\frac{\delta k}{k_r}\right)\sqrt{(f_0+f_\tau')^2+\left(\frac{cf_a}{2v}\right)^2}-\frac{\delta k}{k_r}f_0-\Delta f_0}\right)-\frac{4\pi}{c}R_{ref}\left(f_0+f_\tau'\right) \tag{65}$$

According to (34), (35), and (65), we can easily simplify the 2-D phase error as follows:

$$\begin{aligned}\Phi_e &= \Phi_{\text{Stolt}}-\Phi_{\text{ideal}}\\ &= K_y\cdot\left\{\left[\left(1+\frac{\delta k}{k_r}\right)\sqrt{1+u^2}-m\right]\cdot\left[\zeta\left(\frac{u}{(1+\frac{\delta k}{k_r})\sqrt{1+u^2}-m}\right)-\frac{c\cdot\Delta t}{2}\right]-v\cdot u\cdot\vartheta\left(\frac{u}{(1+\frac{\delta k}{k_r})\sqrt{1+u^2}-m}\right)-r_p+u\cdot x_p\right\}.\end{aligned} \tag{66}$$

Although there are some differences between (36) and (66), they can both be simplified into the same representation as (37), except that the specific form of $\xi(\cdot)$ has to do some modification.

REFERENCES

[1] I. G. Cumming and F. H. Wong, *Digital Signal Processing of Synthetic Aperture Radar Data: Algorithms and Implementation*. Norwood, MA, USA: Artech House, 2004.

[2] J. P. Yao, "Microwave photonics," *J. Lightw. Technol.*, vol. 27, no. 3, pp. 314–225, Mar. 2009.

[3] S. A. Pappert, "RF photonics: Status, challenges and opportunities," in *Proc. IEEE Avion, Fiber-Opt. Photon. Technol. Conf.*, 2011, pp. 7–8.

[4] L. Shuguang, S. Ouyang, Z. Kuai, S. Shi, and L. Zhu, "Design and analysis of LFMCW radar with the signal based on microwave photonic generation," in *Proc. 2nd China Int. SAR Symp.*, 2021, pp. 1–4.

[5] J. Capmany and D. Novak, "Microwave photonics combines two worlds," *Nature Photon.*, vol. 1, pp. 319–330, 2007.

[6] S. L. Pan, D. Zhu, and F. Z. Zhang, "Microwave photonics for modern radar systems," *Trans. Nanjing Univ. Aeronaut. Astron.*, vol. 31, no. 3, pp. 219–240, 2014.

[7] A. Meta, P. Hoogeboom, and L. P. Ligthart, "Signal processing for FMCW SAR," *IEEE Trans. Geosci. Remote Sens.*, vol. 45, no. 11, pp. 3519–3532, Nov. 2007.

[8] W. Glenn, "Noise in interferometric optical systems: An optical Nyquist theorem," *IEEE J. Quantum Electron.*, vol. 25, no. 6, pp. 1218–1224, Jun. 1989.

[9] W. Xu, B. Wang, M. Xiang, R. Li, and W. Li, "Image Defocus in an airborne UWB VHR microwave photonic SAR: Analysis and compensation," *IEEE Trans. Geosci. Remote Sens.*, vol. 60, 2022, Art. no. 5213518.

[10] M. Desai and W. Jenkins, "Convolution backprojection image reconstruction for spotlight mode synthetic aperture radar," *IEEE Trans. Image Process.*, vol. 1, no. 4, pp. 505–517, Oct. 1992.

[11] R. Raney, H. Runge, R. Bamler, I. Cumming, and F. Wong, "Precision SAR processing using chirp scaling," *IEEE Trans. Geosci. Remote Sens.*, vol. 32, no. 4, pp. 786–799, Jul. 1994.

[12] A. Moreira and Y. Huang, "Airborne SAR processing of highly squinted data using a chirp scaling approach with integrated motion compensation," *IEEE Trans. Geosci. Remote Sens.*, vol. 32, no. 5, pp. 1029–1040, Sep. 1994.

[13] G. Davidson, I. Cumming, and M. Ito, "A chirp scaling approach for processing squint mode SAR data," *IEEE Trans. Aerosp. Electron. Syst.*, vol. 32, no. 1, pp. 121–133, Jan. 1996.

[14] D. An, X. Huang, T. Jin, and Z. Zhou, "Extended nonlinear chirp scaling algorithm for high-resolution highly squint SAR data focusing," *IEEE Trans. Geosci. Remote Sens.*, vol. 50, no. 9, pp. 3595–3609, Sep. 2012.

[15] G. Sun, M. Xing, Y. Liu, L. Sun, Z. Bao, and Y. Wu, "Extended NCS based on method of series reversion for imaging of highly squinted SAR," *IEEE Geosci. Remote Sens. Lett.*, vol. 8, no. 3, pp. 446–450, May 2011.

[16] E. C. Zaugg and D. G. Long, "Generalized frequency-domain SAR processing," *IEEE Trans. Geosci. Remote Sens.*, vol. 47, no. 11, pp. 3761–3773, Nov. 2009.

[17] C. Cafforio, C. Prati, and F. Rocca, "SAR data focusing using seismic migration techniques," *IEEE Trans. Aerosp. Electron. Syst.*, vol. 27, no. 2, pp. 194–207, Mar. 1991.

[18] A. Reigber, E. Alivizatos, A. Potsis, and A. Moreira, "Extended wavenumber-domain synthetic aperture radar focusing with integrated motion compensation," *Proc. Inst. Elect. Eng.-Radar Sonar Navigat.*, vol. 153, no. 3, pp. 301–310, 2006.

[19] C.-C. Chen and H. C. Andrews, "Target-motion-induced radar imaging," *IEEE Trans. Aerosp. Electron. Syst.*, vol. AES-16, no. 1, pp. 2–14, Jan. 1980.

[20] G. Delisle and H. Wu, "Moving target imaging and trajectory computation using ISAR," *IEEE Trans. Aerosp. Electron. Syst.*, vol. 30, no. 3, pp. 887–899, Jul. 1994.

[21] D. Zhu, L. Wang, Q. Tao, and Z. Zhu, "ISAR range alignment by minimizing the entropy of the average range profile," in *Proc. IEEE Radar Conf.*, 2006, pp. 813–818.

[22] D. Zhu, L. Wang, Y. Yu, Q. Tao, and Z. Zhu, "Robust ISAR range alignment via minimizing the entropy of the average range profile," *IEEE Geosci. Remote Sens. Lett.*, vol. 6, no. 2, pp. 204–208, Apr. 2009.

[23] J. Chen, M. Xing, H. Yu, B. Liang, J. Peng, and G.-C. Sun, "Motion compensation/autofocus in airborne synthetic aperture radar: A review," *IEEE Geosci. Remote Sens. Mag.*, vol. 10, no. 1, pp. 185–206, Mar. 2022.

[24] C. Mancill and J. Swiger, "A map drift autofocus technique for correcting higher order SAR phase errors," in *Proc. Rec. 27th Annu. Tri-Service Radar Symp.*, 1981, pp. 391–400.

[25] P. Samczynski and K. S. Kulpa, "Coherent MapDrift technique," *IEEE Trans. Geosci. Remote Sens.*, vol. 48, no. 3, pp. 1505–1517, Mar. 2010.

[26] O. O. Bezvesilniy, I. M. Gorovyi, and D. M. Vavriv, "Estimation of phase errors in SAR data by local-quadratic map-drift autofocus," in *Proc. 13th Int. Radar Symp.*, 2012, pp. 376–381.

[27] L. Zhang, M. Hu, G. Wang, and H. Wang, "Range-dependent map-drift algorithm for focusing UAV SAR imagery," *IEEE Geosci. Remote Sens. Lett.*, vol. 13, no. 8, pp. 1158–1162, Aug. 2016.

[28] D. Wahl, P. Eichel, D. Ghiglia, and C. Jakowatz, "Phase gradient autofocus-a robust tool for high resolution SAR phase correction," *IEEE Trans. Aerosp. Electron. Syst.*, vol. 30, no. 3, pp. 827–835, Jul. 1994.

[29] W. Ye, T. S. Yeo, and Z. Bao, "Weighted least-squares estimation of phase errors for SAR/ISAR autofocus," *IEEE Trans. Geosci. Remote Sens.*, vol. 37, no. 5, pp. 2487–2494, Sep. 1999.

[30] W. Van Rossum, M. Otten, and R. Van Bree, "Extended PGA for range migration algorithms," *IEEE Trans. Aerosp. Electron. Syst.*, vol. 42, no. 2, pp. 478–488, Apr. 2006.

[31] D. Zhu, R. Jiang, X. Mao, and Z. Zhu, "PGA multi-subaperture for SAR autofocusing," *IEEE Trans. Aerosp. Electron. Syst.*, vol. 49, no. 1, pp. 468–488, Jan. 2013.
[32] A. Evers and J. A. Jackson, "A generalized phase gradient autofocus algorithm," *IEEE Trans. Comput. Imag.*, vol. 5, no. 4, pp. 606–619, Dec. 2019.
[33] X. Mao, X. He, and D. Li, "Knowledge-aided 2-D autofocus for spotlight SAR range migration algorithm imagery," *IEEE Trans. Geosci. Remote Sens.*, vol. 56, no. 9, pp. 5458–5470, Sep. 2018.
[34] X. Mao and D. Zhu, "Two-dimensional autofocus for spotlight SAR polar format imagery," *IEEE Trans. Comput. Imag.*, vol. 2, no. 4, pp. 524–539, Dec. 2016.
[35] W. G. Carrara, R. S. Goodman, and R. M. Majewski, *Spotlight Synthetic Aperture Radar: Signal Processing Algorithms*. Norwood, MA, USA: Artech House, 1995.
[36] C. Esposito, A. Natale, G. Palmese, P. Berardino, and S. Perna, "Geometric distortions in FMCW SAR images due to inaccurate knowledge of electronic radar parameters: Analysis and correction by means of corner reflectors," *Remote Sens. Environ.*, vol. 232, 2019, Art. no. 111289.
[37] M. Kirscht, "Detection and imaging of arbitrarily moving targets with single-channel SAR," *Proc. Inst. Elect. Eng.—Radar Sonar Navigat.*, vol. 150, no. 1, pp. 7–11, 2003.
[38] R. Li et al., "An ultrahigh-resolution continuous wave synthetic aperture radar with photonic-assisted signal generation and dechirp processing," in *Proc. 17th Eur. Radar Conf.*, 2021, pp. 13–16.
[39] D. Meng, D. Hu, and C. Ding, "A new approach to airborne high resolution SAR motion compensation for large trajectory deviations," *Chin. J. Electron.*, vol. 21, no. 4, pp. 764–769, 2012.

Min Chen was born in Henan Province, China, in 1998. She received the B.S. degree in Internet of Things engineering from Shandong University, Jinan, China, in 2020. She is currently working toward the Ph.D. degree with the Aerospace Information Research Institute, Chinese Academy of Sciences, Beijing, China.

Her current research interests include synthetic aperture radar (SAR) 2-D imaging and SAR autofocus.

Xiaolan Qiu (Senior Member, IEEE) was born in 1982. She received the B.S. degree in electronic engineering and information science from the University of Science and Technology of China, Hefei, China, in 2004, and the Ph.D. degree in signal and information processing from the Graduate University of Chinese Academy of Sciences, Beijing, China, in 2009.

Since 2009, she has been with the Aerospace Information Research Institute, Chinese Academy of Sciences. Since 2020, she has also been with the Suzhou Aerospace Information Research Institute, Suzhou, China. Her research was funded by the Excellent Young Scientists Fund of the National Natural Science Foundation of China. Her research interests include synthetic aperture radar 2-D/3-D imaging and microwave vision.

Dr. Qiu is the Associate Editor for IEEE GEOSCIENCE AND REMOTE SENSING LETTERS and a Young Associate Editor for *Journal of Radars*.

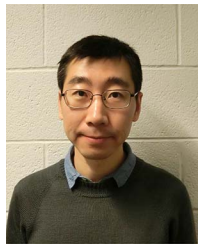

Ruoming Li (Senior Member, IEEE) received the Ph.D. degree in optical engineering from Nanjing University, Nanjing, China, in 2015.

He was a Joint Training Student with the College of Engineering and Applied Sciences, Nanjing University, and also with the School of Electrical Engineering and Computer Science, University of Ottawa, Ottawa, ON, Canada. He is currently an Associate Research Professor with the Aerospace Information Research Institute, Chinese Academy of Sciences, Beijing, China. His research interests include photonic-assisted microwave mixer, photonic-assisted synthetic aperture radar, photon generation of microwave and millimeter-wave signals, and radio over fiber.

Wangzhe Li (Member, IEEE) received the B.E. degree in electronic science and technology from Xi'an Jiaotong University, Xi'an, China, in 2004, the M.Sc. degree in electrical engineering from Tsinghua University, Beijing, China, in 2007, and the Ph.D. degree in electrical engineering from the University of Ottawa, Ottawa, ON, Canada, in 2013.

In 2018, he joined the National Key Laboratory of Microwave Imaging Technology, Chinese Academy of Sciences, Beijing, as the Director. He is currently a Research Professor with the National Key Laboratory of Microwave Imaging Technology, Aerospace Information Research Institute, Chinese Academy of Sciences. His research interests include photonic-assisted synthetic aperture radar, photonic generation of microwave and terahertz signals, arbitrary waveform generation, optoelectronic oscillation, and integrated photonics.

Kun Fu (Senior Member, IEEE) received the B.Sc., M.Sc., and Ph.D. degrees in signal and information processing from the National University of Defense Technology, Changsha, China, in 1995, 1999, and 2002, respectively.

He is currently a Professor with the Aerospace Information Research Institute, Chinese Academy of Sciences, Beijing, China. His research interests include computer vision, remote sensing image understanding, geospatial data mining, and visualization.